

# Mono-stable hydromagnetic stellar differential rotation

B. B. Karak<sup>1</sup>, P. J. Käpylä<sup>2,3</sup>, M. J. Mantere<sup>3</sup>, and A. Brandenburg<sup>1,4</sup>

<sup>1</sup> NORDITA, KTH Royal Institute of Technology and Stockholm University, Roslagstullsbacken 23, SE-10691 Stockholm, Sweden

<sup>2</sup> Department of Physics, Gustaf Hållströmin katu 2a (PO Box 64), FI-00014 University of Helsinki, Finland

<sup>3</sup> ReSoLVE Centre of Excellence, Department of Information and Computer Science, Aalto University, PO Box 15400, FI-00076 Aalto, Finland

<sup>4</sup> Department of Astronomy, Stockholm University, SE-10691 Stockholm, Sweden

Received ? / Accepted ?, Revision: 1.220

## ABSTRACT

**Context.** Late-type stars rotate differentially owing to anisotropic turbulence in their outer convection zones. The rotation is called solar-like (SL) when the equator rotates fastest and anti-solar (AS) otherwise. Hydrodynamic simulations explain a transition from SL to AS rotation as the influence of rotation on convection is reduced, but the opposite transition occurs at a different point in the parameter space. The system is bistable, i.e., SL and AS rotation profiles can both be stable.

**Aims.** We study the effect of a dynamo-generated magnetic field on the large-scale flows, particularly on the possibility of bistable behavior of differential rotation.

**Methods.** We solve the hydromagnetic equations numerically in a rotating spherical shell up to  $\pm 75^\circ$  latitude (wedge geometry) for a set of different radiative conductivities controlling the relative importance of convection.

**Results.** A transition from SL to AS rotation is confirmed, but there is no bistability due to a strong influence of self-consistently generated magnetic fields on the differential rotation. In all cases, both differential rotation and meridional circulation have significant magnetic cycle related variations that are comparable to the solar observations. AS rotation profiles are obtained when the rotational influence on convection is weak, although magnetic cycles are more regular than for SL rotation.

**Conclusions.** Purely hydrodynamic simulations of differential rotation are shown to be of limited relevance as magnetic fields, self-consistently generated by dynamo action, significantly affect the rotation profiles.

**Key words.** convection – turbulence – Sun: magnetic fields Sun: rotation – stars: rotation

## 1. Introduction

Differential rotation is an important ingredient for the generation of stellar magnetic fields. The internal rotation rate of the Sun has been mapped by helioseismology, revealing that the angular velocity within the convection zone mildly increases (decreases) as a function of radius at low (high) latitudes and that the radial shear is concentrated in shallow layers at the base of the convection zone and near the surface (e.g., Brown et al. 1989; Schou et al. 1998; Thompson et al. 2003). Thus the solar equator rotates faster than its poles. This kind of rotation profile is called *solar-like* (SL) differential rotation. The opposite case where the equator rotates slower than the poles, is referred to as *anti-solar* (AS) differential rotation. Due to the difficulties in observing slowly rotating stars that might possess AS differential rotation, it is not clear how common it is in main-sequence stars. However, it has been observed in some K giants (e.g., Strassmeier et al. 2003; Weber et al. 2005).

Historically, the differential rotation and magnetic fields of the Sun and other stars have been modeled by two approaches – mean-field models and global convection simulations. In the mean-field approach, small-scale turbulence is parameterized by expressing the *Reynolds stress* in the momentum equation in terms of the mean velocity, the

*turbulent electromotive force* in the induction equation in terms of the mean magnetic field, and the *turbulent heat flux* in the entropy equation in terms of the mean entropy. These parameterizations involve turbulent transport coefficients that need to be calculated for highly turbulent flows of stellar interiors. Analytical approaches, such as first-order smoothing, involve approximations that are ill-suited for stellar conditions and may yield inaccurate results. A numerical method for determining the turbulent transport coefficients relevant for the electromotive force is the test-field method (Schinnerer et al. 2005, 2007), but for angular momentum or heat transport no similar methods have been developed yet. This means that the turbulent transport coefficients used in mean-field models are often based on educated guesses or they are even used as free parameters. Despite these shortcomings, hydrodynamical mean-field models are capable of producing SL differential rotation (Brandenburg et al. 1992; Kitchatinov & Rüdiger 1995; Rempel 2005; Kitchatinov & Olemskoy 2011) as well as basic properties of the rotation in some other stars (Küker & Rüdiger 2011; Kitchatinov & Olemskoy 2011; Hotta & Yokoyama 2011). However, obtaining AS differential rotation is less straightforward for mean-field models (e.g., Kitchatinov & Rüdiger 2004). At the same time, mean-field dynamo models also reproduce some features of solar and stellar magnetic

Send offprint requests to: e-mail: [bbkarak@nordita.org](mailto:bbkarak@nordita.org)

cycles either by including turbulent inductive effects (Käpylä et al. 2006; Pipin & Kosovichev 2011), or by applying the Babcock-Leighton process in the so-called flux transport dynamo models (e.g., Choudhuri et al. 1995; Dikpati & Charbonneau 1999; Karak 2010; Karak et al. 2014).

On the other hand, there have been some successes in modelling the differential rotation and magnetic fields using global convection simulations, mainly in recent years (Miesch et al. 2006; Ghizaru et al. 2010; Racine et al. 2011; Käpylä et al. 2012, 2013; Augustson et al. 2013; Warnecke et al. 2013). However, due to the extreme parameter regimes of the Sun, realistic simulations are not possible at present. Nevertheless, the simulations are able to reproduce solar values of the Coriolis number  $Co$ , which measures the relative importance of rotation and turbulent convection. For certain values of  $Co$ , but with different values for other parameters such as the fluid and magnetic Reynolds and Prandtl numbers, simulations occasionally produce AS differential rotation (e.g., Matt et al. 2011; Käpylä et al. 2014), poleward migration of the large-scale magnetic fields (Gilman 1983; Käpylä et al. 2010b; Nelson et al. 2013), no clear magnetic cycles (Brown et al. 2010), or sometimes even no appreciable large-scale contribution to the magnetic field (Brun et al. 2004).

According to mean-field hydrodynamics, differential rotation is generated from the anisotropy of the Reynolds stress which is parameterized in terms of the so-called  $\Lambda$ -effect (Rüdiger 1980, 1989). A radially increasing (SL) angular velocity results if horizontal turbulent velocities dominate over vertical ones, while AS rotation follows if radial motions (even laminar ones) are dominant. The importance of the  $\Lambda$ -effect depends on the rotational influence on the turbulence, i.e., the value of  $Co$ , which is the ratio of the convective turnover time to the rotation period. At large  $Co$ , the SL rotation is more favorable and the transition from SL to AS rotation depends on the Coriolis number (Brun & Palacios 2009; Chan 2010; Käpylä et al. 2011a,b; Guerrero et al. 2013; Gastine et al. 2013, 2014). Using Boussinesq convection, Gastine et al. (2014) discovered that near the transition from AS to SL rotation, both states are possible, depending on the initial conditions of the simulations. This has been independently verified by Käpylä et al. (2014) in fully compressible convection simulations. If this discovery were to apply to the Sun, this might have important consequences, because young rapidly rotating stars, which preferably possess SL rotation, slowly spin down due to loss of the angular momentum and can persist in the SL rotation state even when their rotation is slow. Some doubts have already been expressed by Fan & Fang (2014), who found that the bistability disappears when magnetic fields are present.

In the magnetohydrodynamic case the situation is more complicated than in the case of pure hydrodynamics. A dynamically significant magnetic field, which possibly varies cyclically, introduces extra time dependent effects into the system, capable of influencing the fluid flow both through large-scale effect (Malkus-Proctor effect; see Malkus & Proctor 1975; Brandenburg et al. 1992) and small-scale effects (Reynolds and Maxwell stresses and therefore the  $\Lambda$ -effect; see Kitchatinov et al. 1994). Therefore, the magnetic field tries to destabilize the equilibrium states of the rotation. To explore to what extent the presence of a dynamically significant large-scale magnetic

field affects the bistable nature of the differential rotation we perform several simulations with the same setup as in Käpylä et al. (2014), but including magnetic fields. Similar to their work, we perform two types of simulations. In one of them we run the simulations from scratch, i.e., with an initially rigid rotation profile. Then we take either a SL state or an AS state and vary the rotational influence by varying the radiative heat conductivity to identify the transition.

Next we measure the temporal variations of the Lorentz forces (both from large-scale and small-scale contributions) to understand the temporal variations of the large-scale flows observed in the simulations (§ 3.8). Finally, we compute the contributions of the Reynolds stress, Maxwell stress and the mean tension (from the axisymmetric magnetic field) to the angular momentum balance (§ 4). Then we study the influence of the magnetic field on the angular momentum transport by comparing the results with the hydrodynamic simulations.

## 2. The Model

### 2.1. Basic equations

Our model is similar to many earlier studies (Käpylä et al. 2012, 2013; Cole et al. 2014). The hydrodynamic part of this model has been used in Käpylä et al. (2014). We model a spherical wedge with radial, latitudinal, and longitudinal extents  $r_0 \leq r \leq r_1$ ,  $\theta_0 \leq \theta \leq \pi - \theta_0$ , and  $0 \leq \phi \leq \phi_0$ , respectively. Here,  $r_0 = 0.72 R_\odot$  and  $r_1 = 0.97 R_\odot$  are the positions of the bottom and top of the computational domain,  $R_\odot$  is the radius of the Sun,  $\theta_0 = \pi/12$  is the colatitude of the polar cap, and  $\phi_0 = \pi/2$  is the longitudinal extent. The following hydromagnetic equations are solved.

$$\frac{\partial \mathbf{A}}{\partial t} = \mathbf{u} \times \mathbf{B} - \mu_0 \eta \mathbf{J}, \quad (1)$$

$$\frac{D \ln \rho}{Dt} = -\nabla \cdot \mathbf{u}, \quad (2)$$

$$\frac{D\mathbf{u}}{Dt} = \mathbf{g} - 2\boldsymbol{\Omega}_0 \times \mathbf{u} + \frac{1}{\rho} (\mathbf{J} \times \mathbf{B} + \nabla \cdot 2\nu\rho\mathbf{S} - \nabla p), \quad (3)$$

$$T \frac{Ds}{Dt} = -\frac{1}{\rho} \nabla \cdot (\mathbf{F}^{\text{rad}} + \mathbf{F}^{\text{SGS}}) + 2\nu\mathbf{S}^2 + \frac{\eta\mu_0}{\rho} \mathbf{J}^2, \quad (4)$$

where  $\mathbf{A}$  is the magnetic vector potential,  $\mathbf{B} = \nabla \times \mathbf{A}$  is the magnetic field,  $\mathbf{J} = \nabla \times \mathbf{B}/\mu_0$  is the current density with  $\mu_0$  being the vacuum permeability,  $\mathbf{u}$  is the velocity,  $D/Dt = \partial/\partial t + \mathbf{u} \cdot \nabla$  is the advective derivative,  $\rho$  is the density,  $s$  is the specific entropy,  $T$  is the temperature,  $p$  is the pressure,  $\nu$  is the constant kinematic viscosity,  $\mathbf{g} = -GM_\odot \mathbf{r}/r^3$  is the gravitational acceleration with  $M_\odot$  being the mass of the Sun,  $\boldsymbol{\Omega}_0 = (\cos \theta, -\sin \theta, 0)\Omega_0$  is the angular velocity vector,  $\mathbf{S}_{ij} = \frac{1}{2}(u_{i;j} + u_{j;i}) - \frac{1}{3}\delta_{ij} \nabla \cdot \mathbf{u}$  is the rate of strain tensor, where the semicolons denote covariant differentiation. The radiative and subgrid-scale (SGS) heat fluxes are given by

$$\mathbf{F}^{\text{rad}} = -K\nabla T \quad \text{and} \quad \mathbf{F}^{\text{SGS}} = -\chi_{\text{SGS}}\rho T\nabla s, \quad (5)$$

respectively. Here  $K$  is the radiative heat conductivity and  $\chi_{\text{SGS}}$  is the turbulent heat diffusivity. The latter represents the unresolved convective transport of heat (Käpylä et al. 2013). The fluid obeys the ideal gas law  $p = (\gamma - 1)\rho e$ , where  $\gamma = c_p/c_v = 5/3$  is the ratio of specific heats at constant pressure and volume.

## 2.2. Initial and boundary conditions

The initial hydrostatic state is isentropic, so the temperature is given by

$$\frac{\partial T}{\partial r} = -\frac{GM_\odot/r^2}{c_V(\gamma-1)(n_{\text{ad}}+1)}, \quad (6)$$

where  $n_{\text{ad}} = 1.5$  is the polytropic index and the value of  $\partial T/\partial r$  at  $r = r_0$  is fixed. The density stratification follows from hydrostatic equilibrium. The initial state chosen is not in thermodynamic equilibrium but closer to the final convecting state to reduce the needed computational time to reach a thermally relaxed state. The heat conductivity profile is chosen such that radiative diffusion is responsible for supplying the energy flux into the system. Radiative diffusion becomes progressively less efficient toward the surface (Käpylä et al. 2011a). As in (Käpylä et al. 2013, 2014), this is achieved by taking a depth-dependent polytropic index  $n(r) = \delta n(r/r_0)^{-15} + n_{\text{ad}} - \delta n$  for the radiative conductivity  $K(r) = K_0[n(r) + 1]$ , where the reference conductivity is  $K_0 = (\mathcal{L}/4\pi)c_V(\gamma-1)(n_{\text{ad}}+1)\rho_0\sqrt{GM_\odot R_\odot}$ , with  $\mathcal{L}$  being the non-dimensional luminosity. Note that  $n = n_{\text{ad}}$  at the bottom and  $n \rightarrow n_{\text{ad}} - \delta n$  towards the surface. Hence,  $K$  decreases toward the surface like  $r^{-15}$  such that the value of  $\delta n$  regulates the flux that is carried by convection (Brandenburg et al. 2005; Käpylä et al. 2014).

Along with the imposed energy flux at the bottom boundary  $F_b = -(K\partial T/\partial r)_{r=r_0}$ , the values of  $\Omega_0$ ,  $\nu$ ,  $\eta$ , and  $\bar{\chi}_{\text{SGS}} = \chi_{\text{SGS}}$  at the middle of the convection zone  $r = r_m = 0.845 R_\odot$  are defined. The turbulent heat conductivity  $\chi_{\text{SGS}}$  is piecewise constant above  $r > 0.75 R_\odot$  with  $\chi_{\text{SGS}} = \bar{\chi}_{\text{SGS}}$  in  $0.75 R_\odot < r < 0.98 R_\odot$ , and  $\chi_{\text{SGS}} = 12.5\bar{\chi}_{\text{SGS}}$  at  $r \geq 0.98 R_\odot$ . At  $r < 0.75 R_\odot$ ,  $\chi_{\text{SGS}}$  tends smoothly to zero (see Fig. 1 of Käpylä et al. 2011a). We fix  $\chi_{\text{SGS}}$  in such a way that at  $r = r_1$  it corresponds to  $5 \times 10^8 \text{ m}^2 \text{ s}^{-1}$  in physical units. We also assume the density and temperature at  $r = r_0$  to have solar values,  $\rho = 200 \text{ kg m}^{-3}$  and  $T = 2.23 \times 10^6 \text{ K}$ .

Radial and latitudinal boundaries are assumed to be impenetrable and stress free for the flow, whereas for the magnetic field we assume a radial field condition on the outer radial boundary and perfect conductor conditions on the lower radial and latitudinal boundaries; see Käpylä et al. (2013) for details. Density and entropy have vanishing first derivatives on the latitudinal boundaries. A black body condition with  $\sigma T^4 = -K\nabla_r T - \chi_{\text{SGS}}\rho T\nabla_r s$ , where  $\sigma$  is related to the Stefan–Boltzmann constant, is applied on the upper radial boundary. However the value of  $\sigma$  is modified to attain the desired values of surface temperature and energy flux. Moreover, we choose  $\sigma$  in such a way that in the initial non-convecting state the flux at the surface carries the total luminosity through the boundary. We use small-scale low amplitude Gaussian noise as initial condition for the velocity and magnetic fields.

As discussed by Käpylä et al. (2013, 2014), in our fully compressible simulation the time step is severely limited if we were to use the solar luminosity. This would imply both huge Rayleigh and small Mach numbers. This problem is avoided by taking an about  $10^6$  times higher luminosity in the simulation than in the Sun. However, the convective velocity  $u$  becomes then in our simulation 100 times larger than in the Sun because the convective energy flux  $F_{\text{conv}}$  scales as  $\rho u^3$ . Therefore to achieve the same rotational influence on the flow as in the Sun, we need to increase  $\Omega$  by the

same factor. Consequently, we have the relations:  $\Omega_{\text{sim}} = (L_0/L_\odot)^{1/3}\Omega_\odot$  and  $\mathbf{u}_{\text{sim}} = (L_0/L_\odot)^{1/3}\mathbf{u}_\odot$ , where  $L_0$  is the luminosity in simulation,  $L_\odot \approx 3.84 \times 10^{26} \text{ W}$  is the solar luminosity, and  $\Omega_\odot$  is the average solar rotation rate  $\approx 2.7 \times 10^{-6} \text{ s}^{-1}$ . Finally the results are scaled back to solar values. All computations are performed with the PENCIL CODE.<sup>1</sup>

## 2.3. Dimensionless parameters and diagnostics

First, we define the non-dimensional input parameters. The luminosity parameter  $\mathcal{L}$  and the normalized pressure scale height at the surface  $\xi$  are given by

$$\mathcal{L} = \frac{L_0}{\rho_0(GM_\odot)^{3/2}R_\odot^{1/2}}, \quad \xi = \frac{(\gamma-1)c_V T_1}{GM_\odot/R_\odot}, \quad (7)$$

where  $T_1$  is the temperature at the surface. The influence of rotation is measured by the Taylor number,

$$\text{Ta} = (2\Omega_0 \Delta r^2/\nu)^2, \quad (8)$$

where  $\Delta r = r_1 - r_0$  is the thickness of the convecting shell. The fluid, magnetic, and SGS Prandtl numbers are defined as

$$\text{Pr} = \frac{\nu}{\chi_m}, \quad \text{Pm} = \frac{\nu}{\eta}, \quad \text{Pr}_{\text{SGS}} = \frac{\nu}{\bar{\chi}_{\text{SGS}}}, \quad (9)$$

respectively, where  $\chi_m = K(r_m)/c_P\rho_m$  is the thermal diffusivity and  $\rho_m$  is the density, both evaluated at  $r = r_m$ . Furthermore, we define the non-dimensional viscosity,

$$\tilde{\nu} = \frac{\nu}{\sqrt{GM_\odot R_\odot}}, \quad (10)$$

and the Rayleigh and convective Rossby numbers (Gilman 1977),

$$\text{Ra} = \frac{GM_\odot(\Delta r)^4}{\nu\bar{\chi}_{\text{SGS}}R_\odot^2} \left( -\frac{1}{c_P} \frac{ds}{dr} \right)_{r_m}, \quad \text{Ro}_c = \left( \frac{\text{Ra}}{\text{Pr}_{\text{SGS}}\text{Ta}} \right)^{1/2}, \quad (11)$$

where the entropy gradient of the non-convecting hydrostatic solution is evaluated in the middle of the convection zone,  $r = r_m$ . We also quote the initial density contrast  $\Gamma_\rho^{(0)} \equiv \rho(r_0)/\rho(r_1)$ .

As diagnostic quantities we define the fluid and magnetic Reynolds numbers, and the Coriolis number as

$$\text{Re} = \frac{u_{\text{rms}}}{\nu k_f}, \quad \text{Rm} = \frac{u_{\text{rms}}}{\eta k_f} = \text{PmRe}, \quad \text{Co} = \frac{2\Omega_0}{u_{\text{rms}}k_f}, \quad (12)$$

where  $u_{\text{rms}} = \sqrt{(3/2)\langle u_r^2 + u_\theta^2 \rangle_{r\theta\phi t}}$  is the volume and time averaged rms velocity during the time when the simulation is thermally relaxed. We exclude  $u_\phi$  from  $u_{\text{rms}}$  as it is dominated by the differential rotation, and use  $k_f = 2\pi/\Delta r$  as an estimate of the wavenumber of the largest eddies. The Taylor number can also be written as  $\text{Ta} = \text{Co}^2 \text{Re}^2 (k_f R_\odot)^4$ .

We define mean values as averages over longitude and time and denote these by an overbar. Sometimes we also perform additional averaging over latitude and/or radius which we always mention explicitly.

<sup>1</sup> <http://pencil-code.google.com/>

**Table 1.** Summary of the runs.

Run	Ra	Pr	$\delta n$	Ro <sub>c</sub>	Re	Co	$\Delta_{\Omega}^{(\theta)}$	$\Delta_{\Omega}^{(r)}$	$\tilde{E}_{\text{kin}}[10^{-7}]$	$E_{\text{mer}}/E_{\text{kin}}$	$E_{\text{rot}}/E_{\text{kin}}$	$\tilde{L}_{\text{rad}}$	$\tilde{L}_{\text{conv}}$	DR	magnetic cycles
A	$3.93 \cdot 10^5$	39.9	2.5	0.73	33	1.34	-0.184	-0.185	0.25	$3.77 \times 10^{-3}$	0.173	0.09	0.95	AS	regular cycle
B	$3.54 \cdot 10^5$	20.3	2.25	0.69	32	1.35	-0.158	-0.143	0.24	$2.87 \times 10^{-3}$	0.134	0.19	0.84	AS	regular cycle
BC	$3.54 \cdot 10^5$	15.6	2.1	0.67	32	1.38	-0.151	-0.134	0.23	$2.69 \times 10^{-3}$	0.155	0.24	0.77	AS	regular cycle
C	$3.16 \cdot 10^5$	13.6	2.0	0.65	30	1.44	0.033	0.014	0.27	$1.05 \times 10^{-3}$	0.341	0.28	0.70	SL	intermittent
D	$2.92 \cdot 10^5$	11.3	1.85	0.63	26	1.67	0.118	0.059	0.26	$0.67 \times 10^{-3}$	0.487	0.33	0.57	SL	irregular cycles
E	$2.77 \cdot 10^5$	10.2	1.75	0.61	25	1.75	0.111	0.057	0.23	$0.81 \times 10^{-3}$	0.468	0.37	0.52	SL	irregular cycles
D0	$2.92 \cdot 10^5$	11.3	1.85	0.63	26	1.67	0.118	0.059	0.26	$0.67 \times 10^{-3}$	0.487	0.33	0.57	SL	irregular cycles
D1	$3.16 \cdot 10^5$	13.6	2.00	0.65	30	1.46	0.013	0.008	0.29	$1.53 \times 10^{-3}$	0.333	0.28	0.71	SL	irregular cycle
D2	$3.31 \cdot 10^5$	15.7	2.10	0.67	31	1.40	-0.069	-0.074	0.21	$1.70 \times 10^{-3}$	0.121	0.24	0.76	AS	irregular cycle
D3	$3.47 \cdot 10^5$	18.5	2.20	0.68	32	1.38	-0.153	-0.140	0.23	$2.69 \times 10^{-3}$	0.143	0.20	0.81	AS	regular cycles
D4	$3.62 \cdot 10^5$	22.5	2.30	0.70	32	1.36	-0.167	-0.158	0.24	$3.17 \times 10^{-3}$	0.149	0.17	0.86	AS	regular cycle
A0	$3.93 \cdot 10^5$	39.9	2.5	0.73	33	1.34	-0.184	-0.185	0.25	$3.77 \times 10^{-3}$	0.173	0.09	0.95	AS	regular cycle
A1	$3.85 \cdot 10^5$	33.3	2.45	0.72	32	1.36	-0.172	-0.184	0.25	$3.57 \times 10^{-3}$	0.163	0.11	0.92	AS	regular cycle
A2	$3.78 \cdot 10^5$	28.5	2.4	0.71	32	1.36	-0.135	-0.144	0.23	$2.93 \times 10^{-3}$	0.122	0.13	0.89	AS	irregular cycles
A3	$3.62 \cdot 10^5$	22.3	2.3	0.70	32	1.38	-0.154	-0.150	0.23	$2.95 \times 10^{-3}$	0.126	0.17	0.85	AS	irregular cycle
A4	$3.47 \cdot 10^5$	18.3	2.2	0.68	32	1.38	-0.141	-0.133	0.23	$2.79 \times 10^{-3}$	0.124	0.20	0.81	AS	irregular cycle
A5	$3.31 \cdot 10^5$	15.5	2.1	0.67	31	1.41	-0.075	-0.073	0.23	$2.04 \times 10^{-3}$	0.142	0.24	0.76	AS	irregular cycle
A6	$3.16 \cdot 10^5$	13.4	2.0	0.65	30	1.44	0.066	0.017	0.24	$1.40 \times 10^{-3}$	0.212	0.28	0.71	SL	irregular cycles
A7	$3.00 \cdot 10^5$	11.9	1.9	0.63	29	1.53	0.091	0.055	0.31	$0.58 \times 10^{-3}$	0.499	0.31	0.62	SL	irregular cycles
A8	$2.85 \cdot 10^5$	10.7	1.8	0.62	27	1.61	0.121	0.073	0.29	$0.61 \times 10^{-3}$	0.553	0.35	0.54	SL	irregular cycles
B'	$3.54 \cdot 10^5$	20.3	2.25	0.69	32	1.34	-0.154	-0.149	0.21	$3.66 \times 10^{-3}$	0.117	0.19	0.82	AS	regular cycle
B''	$3.54 \cdot 10^5$	20.3	2.25	0.69	32	1.36	-0.132	-0.140	0.25	$2.66 \times 10^{-3}$	0.128	0.19	0.85	AS	regular cycle

**Notes.** In all runs,  $\text{Pm} = 1$ ,  $\bar{\chi}_{\text{SGS}} = 3.7 \cdot 10^8 \text{ m}^2 \text{ s}^{-1}$  by taking  $\chi_{\text{SGS}}(r_1) = 5 \cdot 10^8 \text{ m}^2 \text{ s}^{-1}$ ,  $\nu = 9.3 \cdot 10^7 \text{ m}^2 \text{ s}^{-1}$ ,  $\text{Pr}_{\text{SGS}} = 0.25$ ,  $\mathcal{L} = 3.85 \cdot 10^{-5}$ ,  $\text{Ta} = 2.98 \cdot 10^6$ ,  $\xi = 0.0325$  which gives  $\Gamma \approx 12$ ,  $\Omega_0/\Omega_{\odot} = 1$ , and the grid resolution is  $128 \times 256 \times 128$ . The volume and time averaged total kinetic energy is  $\tilde{E}_{\text{kin}} = \langle \frac{1}{2} \rho u^2 \rangle$  in units of  $GM_{\odot} \rho_0 / R_{\odot}$ , whereas the kinetic energy of the meridional circulation is  $E_{\text{mer}} = \frac{1}{2} \langle \rho (\bar{u}_r^2 + \bar{u}_{\theta}^2) \rangle$  and for the differential rotation it is  $E_{\text{rot}} = \frac{1}{2} \langle \rho \bar{u}_{\phi}^2 \rangle$ .  $\tilde{L}_{\text{rad}}$  and  $\tilde{L}_{\text{conv}}$  are the fractions of total flux transported by radiative conduction and resolved convection at the middle of the convection zone. Here, ‘DR’ stands for differential rotation. The last two Runs B’ and B’’ are same as Run B, but with larger ( $\pm 84^\circ$ ) and smaller ( $\pm 66^\circ$ ) latitudinal extents, respectively.

### 3. Results

First, we perform a set of simulations for different values of the radiative conductivity starting from the initial condition described in Sec. 2.2. These are referred to as Runs A–E in Table 1. Except for the allowance of a magnetic field, all other input parameters of our Runs A–E are identical to those of Käpylä et al. (2014). However, we have an additional Run BC in this set, whose radiative conductivity lies between those of Runs B and C. It turns out that Runs A–BC produce AS differential rotation, while Runs C–E produce SL differential rotation. Next, we perform two further sets of runs where we use Runs A and D with AS and SL differential rotation, respectively, as progenitors to study the possibility of bistability of the rotation profile.

#### 3.1. Energy fluxes in our dynamo runs

The radiative conductivity in our model is controlled by the parameter  $\delta n$ , regulating the fractional flux that convection has to transport. Increasing  $\delta n$  reduces the radiative flux and increases the convective flux and thus  $u_{\text{rms}}$ . Having  $\Omega_0$  fixed, changing  $\delta n$  affects the rotational influence on the convection via the convective velocities (for further details see Käpylä et al. 2014). Hence, different values of  $\delta n$  in Runs A–E imply different values of Co. Thus, Run E is more rotationally dominated than Run A. For Run A with  $\delta n = 2.5$ , the convective flux dominates over the other fluxes and the radiative flux transports a very small frac-

tion of the luminosity. For the definitions of the fluxes we refer to Eqs. (26)–(31) of Käpylä et al. (2013).

In the statistically stationary state, the total luminosity  $L_{\text{tot}}(r) = 4\pi r^2 \mathcal{F}_{\text{tot}}(r)$  is constant, where  $\mathcal{F}_{\text{tot}}$  is the time averaged total energy flux. In Fig. 1 we show the radial dependence of the contributions from radiation ( $L_{\text{rad}}$ ) and convection ( $L_{\text{conv}}$ ), as well as kinetic ( $L_{\text{kin}}$ ), viscous ( $L_{\text{visc}}$ ), and subgrid scale ( $L_{\text{SGS}}$ ) energy fluxes in the convection zone for Runs A and E. For comparison we also show the fluxes from the corresponding hydrodynamic simulations of Käpylä et al. (2014) as red lines. We see that for Run A, the convective, kinetic, and SGS energy fluxes have decreased in the lower part of the convection zone in the magnetic case. In Run E there is very little change in the SGS flux and only a small reduction of the convective and kinetic energy fluxes is visible. In Table 1 we show the fractions of the radiative and the convective fluxes at the middle of the convection zone for all the runs. In Runs A, B, and BC, the convective flux is above 75% and the radiative flux is less than 25%. By contrast, Runs C, D, and E have a convective flux of less than 70% and the radiative flux is larger than 25%.

We find that the rms-velocity is well described by a one-third power proportionality to the convective energy flux – at least in the narrow range of parameters studied here; see Fig. 2. This is in agreement with the scaling used in connection with the artificially high luminosities used in our simulations (see also Brandenburg et al. 2005).

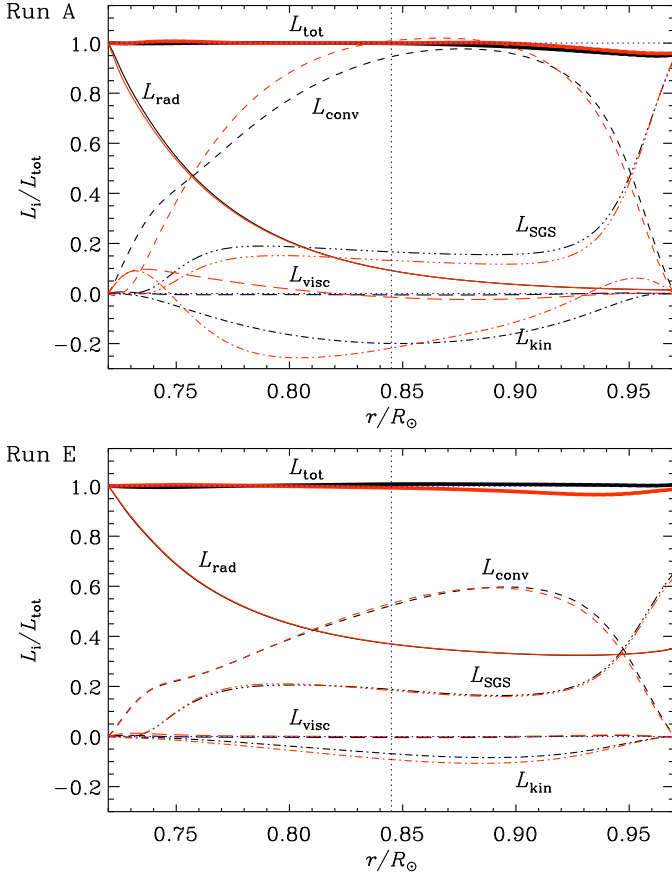


**Fig. 1.** The contributions of different energy fluxes of Run A (top) and E (bottom). The black (red) lines correspond to magnetohydrodynamic (hydrodynamic) case. Thin solid: radiative, dashed: convective, long dashed: viscous, dash-dotted: kinetic energy, dash-triple-dotted: SGS, and thick solid: total. Dotted horizontal lines indicate the zero and unity values. The blue vertical dotted line indicates the position of the middle of the convection zone  $r = r_m$ .

### 3.2. Differential rotation

In Fig. 3 we show the rotation profile  $\bar{\Omega} = \bar{u}_\phi / r \sin \theta + \Omega_0$  for Runs A–E. We see that in Runs A, B, and BC the equator rotates slower than the mid- and high latitudes which is opposite to the rotation profile observed in the Sun. However, we find that the regions near the latitudinal boundaries have slower rotation than mid-latitudes, which was not observed in the hydrodynamical simulations of Käpylä et al. (2014). We have repeated Run B by increasing and decreasing the extent of the latitudinal boundaries. Runs B' and B'' in Table 1 correspond to these two cases where the latitudinal end points are at  $\pm 84^\circ$  and  $\pm 66^\circ$ , respectively. In Fig. 4, we show  $\bar{\Omega}$  profiles for these two runs, whereas in Fig. 5 we show their latitudinal variations at  $r = 0.96R_\odot$ . Looking at these two plots we see that the rotation profiles are very similar in all these runs up to about  $\pm 50^\circ$  latitudes and then there are significant departures near the boundaries. However, the slowly rotating high-latitude branch still exists in all runs. Therefore this is probably not due to our restricted latitudinal extent near the poles, but may be a real feature which might be caused by the magnetic fields. By comparing the rotation profiles from hydrodynamic simulations of Käpylä et al. (2014) for Runs A–E, we see that

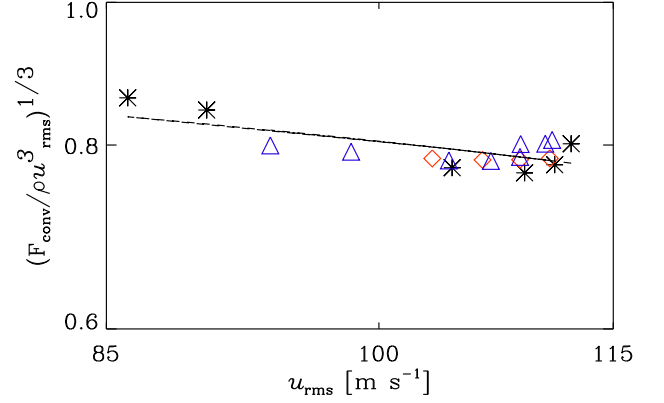


**Fig. 2.** Variation of  $(F_{\text{conv}}/\rho u_{\text{rms}}^3)^{1/3}$  averaged over the whole convection zone as a function of  $u_{\text{rms}}$  from different runs. Black asterisks: Runs A–E, red diamonds: Runs E1–E4, and blue triangles: Runs A1–A8. The dashed line shows the linear dependence between  $u_{\text{rms}}$  and  $(F_{\text{conv}}/\rho u_{\text{rms}}^3)^{1/3}$ .

the pole–equator differential rotation is generally weaker in the magnetic runs, the reduction being strongest in the runs with a slowly rotating equator. This is also reflected in Table 2 where we show the ratio of the rotational energy of the hydrodynamic and magnetic simulations. To illustrate the reduction of differential rotation in the magnetic runs, we show in Fig. 6 the differences in  $\bar{\Omega}$  between the hydrodynamic and magnetic versions of Runs A and E. We see that for Run A the difference is even larger than the actual rotation of the Sun. Possible reasons for the reduction of differential rotation will be discussed in Sec. 4.

In Runs C–E, the equator rotates faster than the polar regions, as is also the case in the Sun. However, unlike some of the nonmagnetic solar-like cases of Käpylä et al. (2014), we never obtain polar vortices or jet-like structures with magnetic fields. It is also interesting to note that the pole–equator difference in the rotational velocity is comparable to that of the Sun. The solar value ( $\sim 430$  nHz) is marked in each colorbar of Fig. 3.

### 3.3. Identifying the SL to AS transition

We measure the relative radial and latitudinal differential rotation by the quantities

$$\Delta_\Omega^{(r)} = \frac{\Omega_{\text{eq}} - \Omega_{\text{bot}}}{\Omega_{\text{eq}}}, \quad \Delta_\Omega^{(\theta)} = \frac{\Omega_{\text{eq}} - \Omega_{55}}{\Omega_{\text{eq}}}, \quad (13)$$

where  $\Omega_{\text{eq}} = \bar{\Omega}(r_1, \pi/2)$  and  $\Omega_{\text{bot}} = \bar{\Omega}(r_0, \pi/2)$  are the equatorial rotation rates at the surface and at the base of the convection zone, and  $\Omega_{55} = \frac{1}{2}[\bar{\Omega}(r_1, 35^\circ) + \bar{\Omega}(r_1, 145^\circ)]$  is the rotation rate at latitudes  $\pm 55^\circ$  computed as an average of  $\bar{\Omega}$  at  $35^\circ$  and  $145^\circ$  co-latitudes on the outer radius. The arrows in the left panel of Fig. 3 show the positions of these points in  $r$ – $\theta$  plane. These quantities, listed in Table 1, help us identify AS and SL differential rotation. SL differential rotation implies  $\Delta_\Omega^{(r)} > 0$  and  $\Delta_\Omega^{(\theta)} > 0$ . Following this definition we see that Runs A, B, and BC are classified as AS and Runs C–E as SL. Hence we see that there is a transition from AS to SL rotation around  $\text{Co} \sim 1.4$ . A similar transition has already been reported by Gastine et al. (2014)

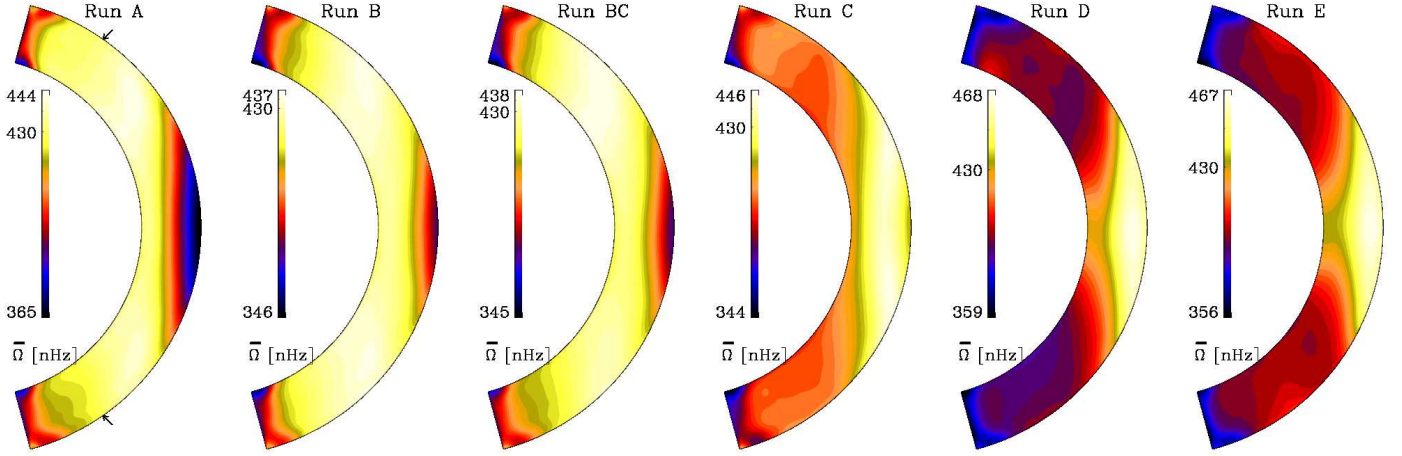


**Fig. 3.** The distribution of angular velocity (in nHz)  $\bar{\Omega}$  in the meridional plane from Runs A–E.  $\bar{\Omega}$  is computed from  $\Omega$  first by the longitudinal average and then the time average over few magnetic cycles. The arrows in the leftmost panel show the co-latitudes at which the latitudinal differential rotation is computed in Eq. (13).

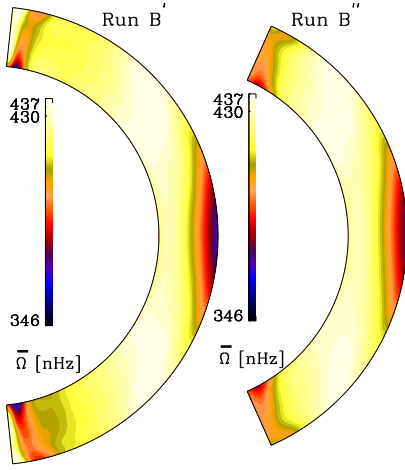


**Fig. 4.** Same as Run B in Fig. 3 but here the latitudinal extent is different. For the left panel the latitudinal boundaries are at  $\pm 84^\circ$ , whereas for the right one they are at  $\pm 66^\circ$ .

and Käpylä et al. (2014). By comparing the current results with the hydrodynamical ones, we see that the transition happens at a slightly smaller value of  $Ro_c$ , also manifested by the change of the AS hydrodynamical counterpart of Run C, to SL in the MHD regime. The transition observed in the current dynamo cases is less abrupt than that of earlier hydrodynamic studies. Therefore we conclude that the magnetic field helps to produce SL differential rotation, which has also been found in the recent anelastic simulations of Fan & Fang (2014).

In Fig. 7 we show differential rotation parameters  $\Delta_\Omega^{(r)}$  and  $\Delta_\Omega^{(\theta)}$  computed from Eq. (13) for all the runs as functions of  $Ro_c$  and  $Ra$ . To compare with the hydrodynamic simulations of Käpylä et al. (2014), we have analyzed the latitudinal differential rotation in their data with our new definition 13. The hydrodynamic values shown in Fig. 7 are now considerably smaller for the AS branch than the ones reported by Käpylä et al. (2014). Note that, had we defined  $\Delta_\Omega^{(\theta)}$  as the difference of rotation between equator

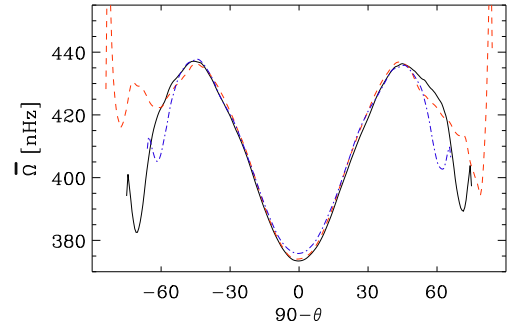


**Fig. 5.** Variations of angular velocities  $\bar{\Omega}$  at  $r = 0.96R_\odot$  from Runs B (solid line), B' (red dashed), and B'' (blue dash-dotted).

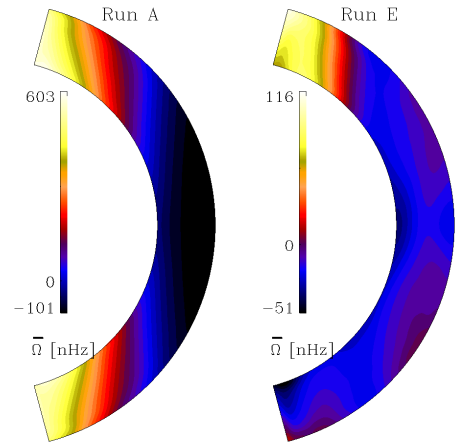


**Fig. 6.** Difference of  $\bar{\Omega}$  between the HD and MHD runs. The left and right panels are for Runs A and E, respectively.

and the endpoints of the domain at  $\theta = \theta_0$  and  $\pi - \theta_0$  as in Käpylä et al. (2013, 2014), instead of  $\Omega_{55}$ , as we do here, we would have obtained smaller values of  $\Delta_\Omega^{(\theta)}$  because of the slowly rotating high latitude regions in



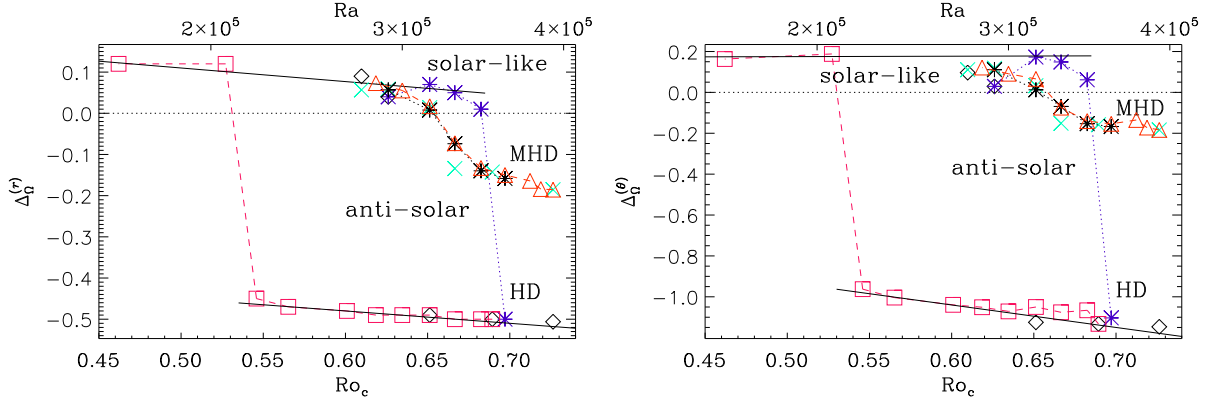


**Fig. 7.** Radial (left panel) and latitudinal (right panel) differential rotation, defined by Eq. (13), for Runs A–E (green crosses), A0–A8 (red dashed line with triangles), and D0–D4 (black asterisks with dotted line). The other points are taken from the hydrodynamical simulations (black diamonds: Runs A–E, blue dotted line with asterisks: Run D0–D4, and red dashed line with squares: Runs B0–B10) of Käpylä et al. (2014). The horizontal black dotted lines in both panels show the zero values of  $\Delta\Omega^{(r)}$  and  $\Delta\Omega^{(\theta)}$ .

our magnetic Runs A–C. Another way of characterizing the SL or AS differential rotation can be done following Käpylä et al. (2011b), who approximated the surface rotation profile in terms of Gegenbauer polynomials, which is,  $\Omega = \Omega_0 \sum_{\ell=1,3,5} \omega_\ell P_\ell^1(\cos \theta) / \sin \theta$ . The sign of  $w_3$  indicates whether a rotation is SL or AS. Following this procedure we obtain the same conclusion for the classification of the SL and AS differential rotation.

#### 3.4. Checking for flow bistability

Next we study the flow bistability by taking AS and SL cases as initial conditions. Firstly, we have performed a set of simulations by starting from the saturated state of Run A with AS differential rotation and decreasing  $\delta n$  slowly, which corresponds to Runs A1–A8 in Table 1. The differential rotation parameters of these runs are shown as red triangles in Fig. 7. Secondly, we start from Run D with SL differential rotation and increase  $\delta n$  slowly to produce Runs D1–D4. These are shown as black asterisks in Fig. 7. We see that both sets of simulations produce similar results and there is no evidence for the existence of multiple solutions at the same parameters. Therefore we conclude that the bistable nature of the differential rotation, recently discovered by Gastine et al. (2014) and Käpylä et al. (2014), disappears when dynamically important magnetic fields are allowed to be generated. This conclusion is supported by the recent study of Fan & Fang (2014) who find a stable SL differential rotation independent of the history of the simulation in their convective dynamo simulations.

#### 3.5. Meridional circulation

For all the AS cases (Runs A, B, and BC) we find single cell meridional circulation with poleward flow near the surface and equatorward flow near the bottom of the convection zone. This is also the usual assumption in flux transport dynamo models (e.g., Dikpati & Charbonneau 1999), although in such models only the equatorward motion at the bottom of the convection zone matters (Hazra et al. 2014). However, as we go to the SL differential rotation cases, i.e., from Run C to Runs D and E, the meridional circulation

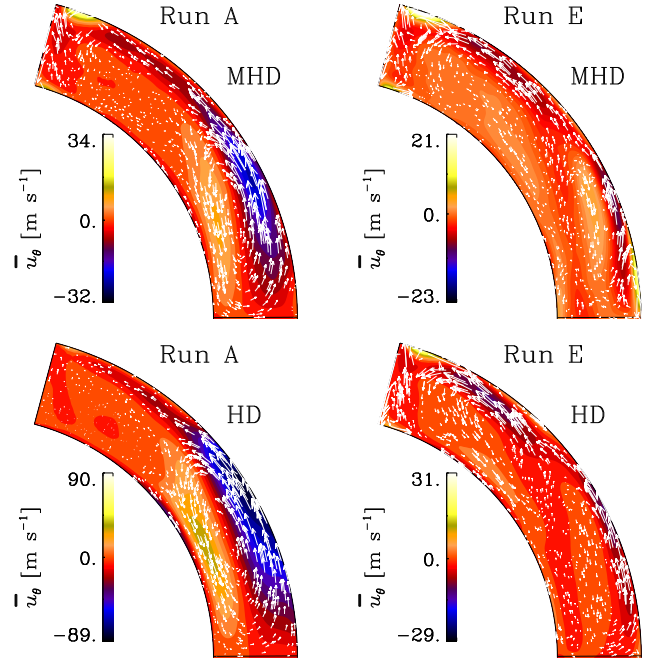


**Fig. 8.** Meridional circulation from Runs A and E. The arrows show the direction of flow  $\bar{\mathbf{u}}_m \equiv (\bar{u}_r, \bar{u}_\theta)$  and the background color shows  $u_\theta$ . Upper (lower) panels are from magnetohydrodynamic (hydrodynamic) simulations.

becomes weaker and shows multiple cells in radius and latitude, which has been detected in recent observations (e.g., Zhao et al. 2013; Schad et al. 2013). Guerrero et al. (2013) also find multi-cell meridional circulation for SL differential rotation and single or two-cell circulation for AS.

Table 1 shows that  $E_{\text{mer}}/E_{\text{kin}}$  decreases rapidly from Runs A to E (with increasing Co the energy in the azimuthal component increases). The upper two panels of Fig. 8 show the meridional circulation for an AS (Run A) and a SL case (Run E). Note that, irrespective of the differential rotation profile, we obtain poleward meridional circulation near the surface and its amplitude is in agreement with solar surface observations (see e.g.,

**Table 2.** Summary of the diagnostic quantities of Runs A–E.

Run	$T_{\text{cyc}}(\text{yr})$	$\overline{B}_{\text{rms}}(\text{G})$	$\frac{E_{\text{mag}}}{E_{\text{kin}}}$	$\frac{E_{\text{pol}}}{E_{\text{kin}}}$	$\frac{E_{\text{tor}}}{E_{\text{kin}}}$	$\frac{E_{\text{mer}}^{\text{HD}}}{E_{\text{mer}}^{\text{MHD}}}$	$\frac{E_{\text{rot}}^{\text{HD}}}{E_{\text{rot}}^{\text{MHD}}}$
A	$5.0 \pm 1.0$	3931	0.119	0.066	0.052	12.1	92.4
B	$10.0 \pm 1.5$	2956	0.068	0.038	0.030	16.1	114.8
BC	$10.0 \pm 1.0$	2724	0.060	0.033	0.026		
C	$7.5 \pm 0.5$	1789	0.028	0.017	0.012	37.6	36.9
D	$4.8 \pm 0.5$	3152	0.120	0.064	0.053	2.2	1.2
E	$6.0 \pm 0.9$	3472	0.156	0.080	0.076	1.9	2.2

**Notes.** Here,  $E_{\text{mag}} = \langle B^2 \rangle / 2\mu_0$  is the total magnetic energy,  $E_{\text{pol}} = \langle (\overline{B}_r^2 + \overline{B}_\theta^2) \rangle / 2\mu_0$  and  $E_{\text{tor}} = \langle \overline{B}_\phi^2 \rangle / 2\mu_0$  are the poloidal and toroidal components of the axisymmetric magnetic energy. All are averaged over volume and time in thermally relaxed state. Last two columns show the ratios of the meridional circulation and rotational energies from hydrodynamic to the magnetic simulations.

Hathaway & Rightmire 2010; Zhao et al. 2013). This suggests that the meridional circulation is not just a consequence of differential rotation, but it must have additional sources such as magnetic fields, differential heating, or differential heat transport.

It is important to compare these results with the hydrodynamical counterparts of the same models shown in the two lower panels. We see that the hydrodynamic flow is much stronger, although the overall pattern is not very different. In Table 2, we compare the energy ratios  $E_{\text{mer}}^{\text{HD}}/E_{\text{mer}}^{\text{MHD}}$  and  $E_{\text{rot}}^{\text{HD}}/E_{\text{rot}}^{\text{MHD}}$  of meridional circulation and rotation respectively with their hydrodynamic counterparts. The magnetic field clearly suppresses the circulation in the AS case whereas in the SL case the effect is small. Moreover, the flow shows significant temporal variation, which will be explored later in § 3.8.

### 3.6. Magnetic cycles and butterfly diagrams

In Fig. 9 we show the time–latitude diagrams of the toroidal field  $\overline{B}_\phi$  (in Gauss) near the surface ( $r = 0.96R_\odot$ ) from Runs A–E. We see that Runs A, B, and BC, which produce AS differential rotation, show prominent magnetic cycles but no clear polarity reversals. For Runs A and B, the cycles are regular and a weak poleward propagation at high latitudes is seen. Another aspect we notice is that, as we go from Run A to Run BC, the magnetic cycles appear at a later time. This is surprising given that the rotation after the turbulence actually increases. For Run C, with SL rotation, the magnetic cycle is rather irregular and shows periods of very weak mean fields. The cycles in Runs D and E are irregular and a different dynamo mode appears to be excited in these simulations, which is also characterized by a weaker influence on the differential rotation than in the AS cases (see the next section).

### 3.7. Diagnostic stellar activity diagrams

The nature of stellar cycles can be characterized by the ratio of cycle frequency  $\omega_{\text{cyc}} = 2\pi/T_{\text{cyc}}$  to  $\Omega_{\text{rot}}$ , where  $T_{\text{cyc}}$  is an estimate of the cycle period. Determining  $T_{\text{cyc}}$  is questionable if the cycle is irregular or the time series not long enough, as is the case for many of the observed cycles of

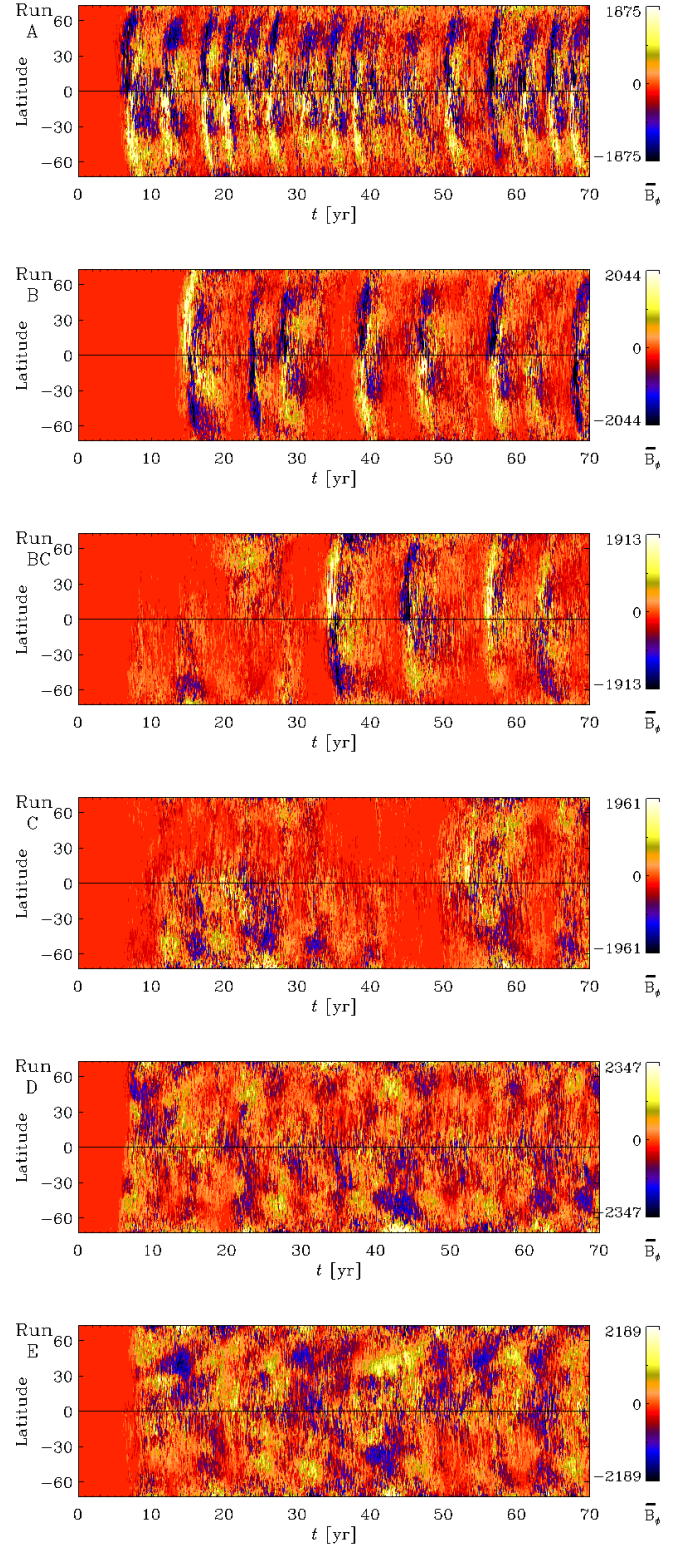


**Fig. 9.** Butterfly diagrams: Contours of the toroidal field  $\overline{B}_\phi$  (in Gauss) at  $r = 0.96 R_\odot$  from Runs A, B, BC, C, D, and E (top to bottom).

stars with activity cycles. Here we compute  $T_{\text{cyc}}$  from the highest peak of the temporal Fourier transform of the time series of  $\overline{B}_\phi$  over  $10^\circ$  to  $50^\circ$  latitudes. Nevertheless, there is a tendency for stars of different characteristics to group at



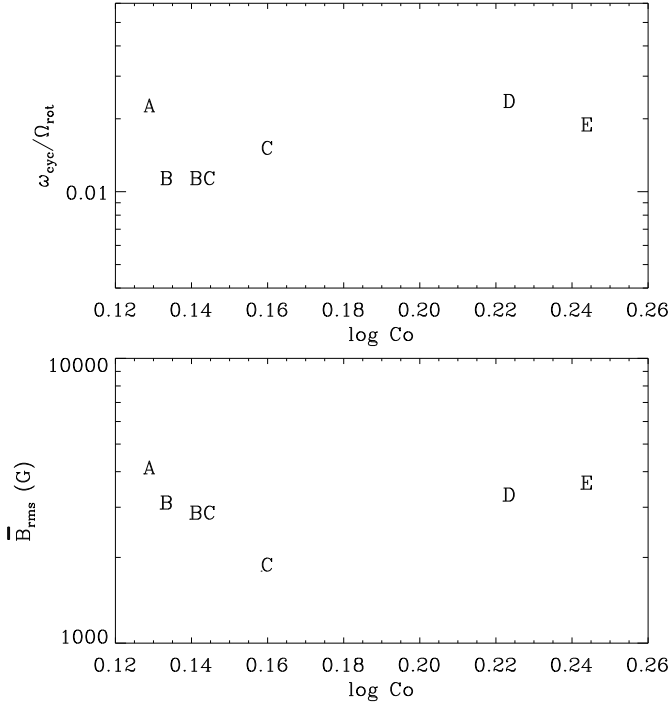


**Fig. 10.** Diagnostic diagram showing  $\omega_{\text{cyc}}/\Omega_{\text{rot}}$  (upper panel) and the strength of the large-scale magnetic field over the whole convection zone measured by  $\overline{B}_{\text{rms}} = \langle \langle B_r \rangle_\phi^2 + \langle B_\theta \rangle_\phi^2 + \langle B_\phi \rangle_\phi^2 \rangle_{r\theta t}^{1/2}$  (lower panel) vs.  $\log \text{Co}$ .

different positions in a “diagnostic” diagram of  $\omega_{\text{cyc}}/\Omega_{\text{rot}}$  versus  $\text{Co}$  (Brandenburg et al. 1998; Saar & Brandenburg 1999). The more rapidly rotating stars of Käpylä et al. (2013) were found to be located in three groups with increasing slope in two of them and decreasing slope in one.

In the present work, the values of  $\text{Co}$  are much smaller, so it is important to repeat such an analysis for the more slowly rotating stars of the present paper. The result is shown in Fig. 10, where we see that stars with AS and SL rotation are located in two different positions in such a diagram. We know that the Sun lies on the upper left branch, but in Fig. 10 this branch corresponds to AS rotation, which obviously disagrees with the observations. However, it is plausible that there are stars with AS rotation that have simply not yet been observed. Our simulations therefore suggest a possible prediction in that such stars might occupy a possibly separate branch further to the left of the solar branch, which already corresponds to the domain of inactive stars. We thus expect there to be either a separate branch or a part of the branch with inactive stars like the Sun, having however AS rotation.

The lower panel of Fig. 10 shows the mean magnetic field. We see that for the AS differential rotation runs (Runs A, B, and BC) the magnetic field decreases with rotation rate, whereas for the SL rotation cases (Runs C, D, and E) it increases.

### 3.8. Magnetic modulation of the flow

We have seen that some of our runs show clear magnetic cycles. Therefore we expect to see a modulation of the flow due to this cyclic variation. In Fig. 11, we show for Run A

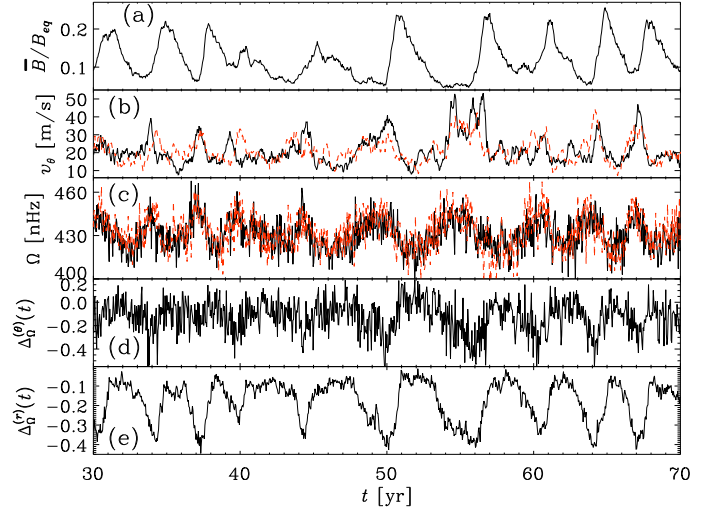


**Fig. 11.** From Run A: (a) The strength of the large-scale magnetic field over the whole convection zone measured by  $\overline{B} = \langle \langle B_r \rangle_\phi^2 + \langle B_\theta \rangle_\phi^2 + \langle B_\phi \rangle_\phi^2 \rangle_{r\theta}^{1/2} / B_{\text{eq}}$ , (b) the strength of the meridional circulation shown by its latitudinal component  $u_\theta$  (smoothed over 5 months), (c) longitudinal averaged angular frequency  $\Omega$ . Both  $u_\theta$  and  $\Omega$  are shown at  $\pm 32^\circ$  latitudes and  $r \approx 0.95 R_\odot$ . The red dashed (black solid) line corresponds to southern (northern) hemisphere. (d) The radial shear  $\Delta_\Omega^{(r)}$ , and (e) the latitudinal shear  $\Delta_\Omega^{(\theta)}$  as functions of time.

the temporal variation of the mean magnetic field ( $\overline{B}$ ) normalized by  $B_{\text{eq}}$ , the latitudinal component of the meridional circulation  $u_\theta$ , the angular frequency  $\Omega$ , and the latitudinal and radial differential rotation  $\Delta_\Omega^{(r)}$  and  $\Delta_\Omega^{(\theta)}$ , defined in Eq. (13). Here  $u_\theta$  and  $\Omega$  are computed at  $\pm 32^\circ$  latitude near the surface in both the northern and southern hemispheres. We see that the meridional circulation has a clear cyclic variation with the magnetic cycle, becoming weaker during cycle maximum and stronger during minimum, the overall temporal variation being about 50% in this case. This kind of anti-correlation between the magnetic cycle and the meridional flow has been found in solar observations (Chou & Dai 2001; Hathaway & Rightmire 2010) and is believed to arise from the Lorentz force of the dynamo-generated magnetic fields (see e.g., Rempel 2006; Karak & Choudhuri 2012). We see that differential rotation also has a clear anti-correlation with the magnetic cycle. It is again anti-correlated with the magnetic cycle. We see that the strong magnetic fields during cycle maxima change  $\Omega$  by a few per cent ( $\approx 6\%$ ) while the variation in shear,  $\Delta_\Omega^{(r)}$  and  $\Delta_\Omega^{(\theta)}$ , can be as large as  $\sim 200\%$ .

We have seen that Runs B, BC, and C produce clear magnetic cycles similar to Run A and in all these runs we do see a clear cycle-dependent variation in the flow. However, for Runs C, D, and E, which produce SL differential rotation, the magnetic cycles are not so regular. In Fig. 12, we show the temporal variations for the SL differential rotation case Run E. We see that the magnetic field does not have a regular cycle. The meridional circulation does not appear to show a clear correlation with the magnetic field, although significant variations exist. The variation is about 50%. Such irregular variation in meridional circulation is

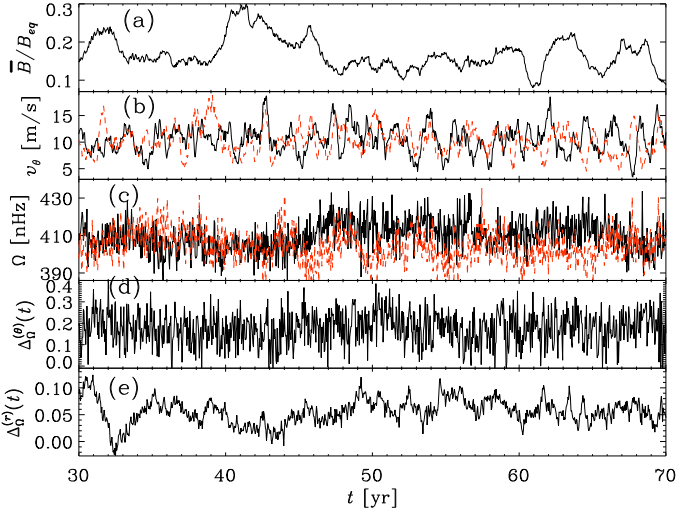


**Fig. 12.** Same as Fig. 11 but from Run E which produces SL differential rotation.

found to be crucial in modeling many aspects of the solar cycle in flux transport dynamo model (Karak & Choudhuri 2011, 2013). The situation is similar in the case of differential rotation and rotational shear: the early part of the time series ( $t = 30 \dots 50$  yr) show an anticorrelation with the magnetic field strength, but at later times this correlation is not so obvious. The variation in differential rotation is about 5%, whereas for the radial and latitudinal shear it is about 60% and 75%, respectively.

Significant variations observed in the large-scale flows in all the simulations motivate us to measure the Lorentz force. The Lorentz force can change the flow by acting in two ways, through large-scale and small-scale magnetic fields. Firstly, it can act directly on the large-scale flow which is known as ‘macro-feedback’ (caused by the mean Lorentz force); see the application of this in many mean-field models, e.g., Schüssler (1979); Brandenburg et al. (1992). Secondly, it can affect the large-scale flow by affecting the convective motions and the best example of this is the magnetic quenching of the  $\Lambda$ -effect, which is known as ‘micro-feedback’ (for an application, see Küker et al. 1999). To get an idea of these effects we measure the  $\phi$ -components of the Lorentz force from the large-scale magnetic fields  $\langle \mathbf{J} \times \mathbf{B} \rangle_\phi$ , and the small-scale contribution  $\langle \mathbf{j} \times \mathbf{b} \rangle_\phi$  which are shown in Fig. 13 both during magnetic maximum (left two panels) and minimum (right two panels) from Run A. We see that the small-scale Lorentz force, which enters into the total stress and thus the  $\Lambda$  effect, is much stronger than the Lorentz force of the large-scale fields and both have significant temporal variations, becoming much weaker during magnetic minimum. Clearly both contributions are responsible of producing temporal variations in the large-scale flows.

#### 4. Turbulent angular momentum transport

Next we compute the contributions of the Reynolds stress  $Q_{ij} = \overline{u'_i u'_j}$  and the Maxwell stress  $M_{ij} = (\rho \mu_0)^{-1} \overline{B'_i B'_j}$  to the angular momentum balance in the convection zone. Here, primes denote fluctuating quantities which are calculated by subtracting the longitudinal mean from the original quantity, e.g.,  $u'_i = u_i - \overline{u}_i$ . The radial and latitudinal

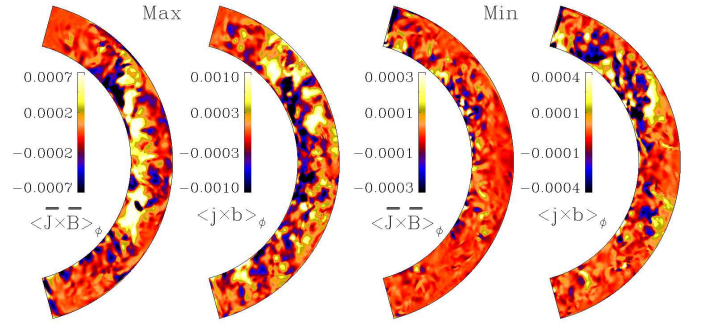


**Fig. 13.** From Run A: Contributions of the  $\phi$ -component of the large-scale Lorentz force  $\mathbf{J} \times \mathbf{B}_\phi$  and small-scale Lorentz force  $\mathbf{j} \times \mathbf{b}$  during a magnetic maximum (left two panels) and minimum (right two panels).

angular momentum transports are determined by the off-diagonal components of  $Q_{ij}$  and  $M_{ij}$ , namely  $Q_{r\phi}$ ,  $Q_{\theta\phi}$ ,  $M_{r\phi}$  and  $M_{\theta\phi}$ , respectively. In the mean-field theory of hydrodynamics, the Reynolds stress contributions to angular momentum transport are approximated in terms of the turbulent viscosity  $\nu_t$  and the  $\Lambda$ -effect (Rüdiger 1980, 1989):

$$Q_{r\phi} = \overline{u'_r u'_\phi} \equiv \Lambda_V \sin \theta \overline{\Omega} - \nu_t r \sin \theta \frac{\partial \overline{\Omega}}{\partial r}, \quad (14)$$

$$Q_{\theta\phi} = \overline{u'_\theta u'_\phi} \equiv \Lambda_H \cos \theta \overline{\Omega} - \nu_t \sin \theta \frac{\partial \overline{\Omega}}{\partial \theta}. \quad (15)$$

The coefficients  $\Lambda_V$  and  $\Lambda_H$  are the vertical and horizontal  $\Lambda$ -effects, which are non-diffusive contributions to the Reynolds stress that arise from the interaction of anisotropic turbulence and rotation (Kitchatinov & Rüdiger 1995). As in earlier work (Käpylä et al. 2014), we adopt the mixing length formula to estimate  $\nu_t$

$$\nu_t = \frac{1}{3} u_{\text{rms}} \alpha_{\text{MLT}} H_p, \quad (16)$$

where  $\alpha_{\text{MLT}} = 1.7$  and  $H_p(r) = -(\partial \ln p / \partial r)^{-1}$ . By computing  $u_{\text{rms}} = u_{\text{rms}}(r, \theta)$  using  $\phi$  averages, we get the profile of  $\nu_t$  in the meridional plane. The two leftmost panels of Fig. 14 show  $Q_{r\phi}$  and  $Q_{\theta\phi}$  normalized by  $\nu_t \Omega_0$ , and the third panel shows  $\nu_t$  normalized by the microphysical viscosity  $\nu$  from Run A. The magnetic field is expected to change the total (Reynolds and Maxwell) stress over the magnetic cycle. In the following, we focus our discussion on the Reynolds stress, whose variation gives the dominant contributions. In fact, magnetic quenching of the Reynolds stress is known to have important consequences in mean-field models, particularly in connection with explaining the origin of the torsional oscillation of the Sun or grand minima (e.g., Kitchatinov et al. 1999; Küker et al. 1999). Therefore, to see the variations over the magnetic cycle, we show  $Q_{r\phi}$  and  $Q_{\theta\phi}$  both during maximum and minimum phases. Note that these are not computed from one snapshot, but from averages over four maxima or minima phases. By comparing top and bottom panels we find that  $Q_{r\phi}$  is slightly stronger during magnetic maximum, although  $Q_{\theta\phi}$  is weaker. We see that  $Q_{r\phi}$  is negative in the middle of the convection zone. This is in agreement with Rieutord et al. (1994) and Käpylä et al. (2014). On the other hand, the latitudinal stress  $Q_{\theta\phi}$  is positive (negative) in the northern (southern) hemisphere, which implies

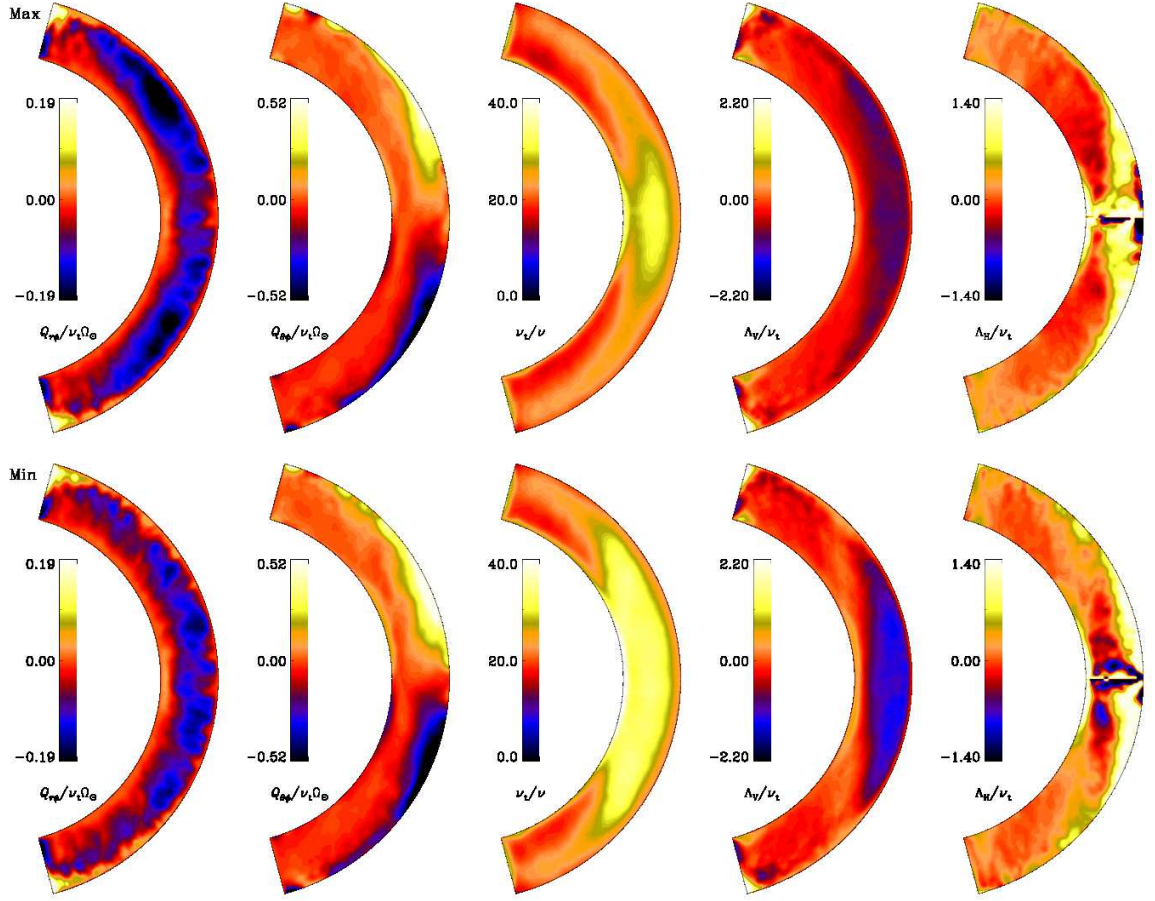


**Fig. 14.** Normalized profiles of  $Q_{r\phi}$ ,  $Q_{\theta\phi}$ ,  $\nu_t$ ,  $\Lambda_V$ , and  $\Lambda_H$  for Run A. The top and bottom panels show data averaged over four cycle maxima and minima, respectively.

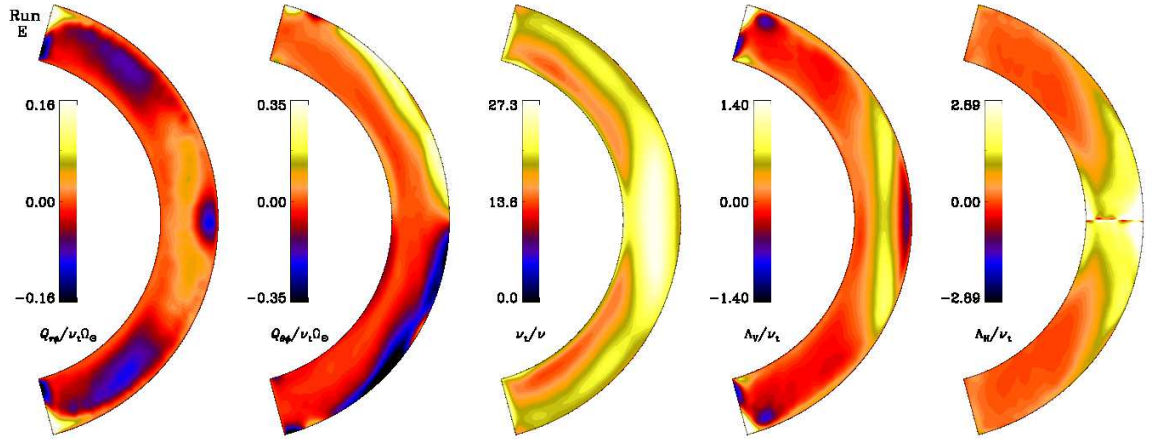


**Fig. 15.** Similar to Fig. 14, but for Run E and time-averaged over many cycles including maxima and minima.

equatorward angular momentum transport. This is true for both Runs A and E (Figs. 14 and 15).

Next, we see in the middle panels of Fig. 14 that  $\nu_t$  is significantly weaker during maximum due to magnetic quenching. The value is around 40, which is similar to the value of  $Re$ . We note that the value of  $\nu_t$  decreases towards high latitudes, but increases towards the deeper regions of the convection zone.

After solving Eqs. (14) and (15) for  $\Lambda_V$  and  $\Lambda_H$  by using the computed values of  $Q_{r\phi}$ ,  $Q_{\theta\phi}$ , and  $\nu_t$ , we find  $\Lambda_V$

and  $\Lambda_H$  again during magnetic maximum and minimum. These are shown in the last two panels of Fig. 14. We see that  $\Lambda_V$  is negative in most of the convection zone, which is in agreement with the findings from the first-order smoothing approximation (Kitchatinov & Rüdiger 1995, 2005), and with earlier numerical studies (e.g., Pulkkinen et al. 1993; Käpylä et al. 2004; Rüdiger et al. 2005; Käpylä & Brandenburg 2008; Käpylä et al. 2014). However, for Run E with SL rotation,  $\Lambda_V$  is positive at low latitudes and does not change much from maximum to



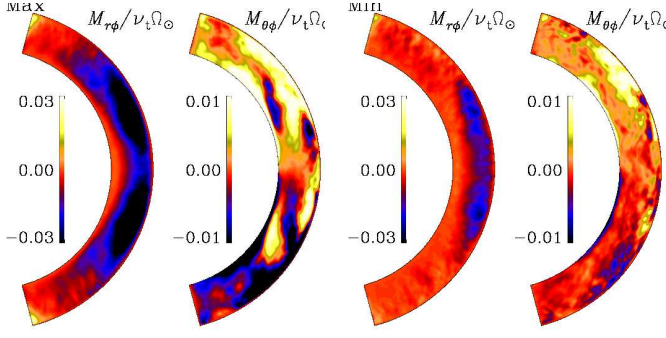


**Fig. 16.** From Run A: Maxwell stress components:  $M_{r\phi}$  and  $M_{\theta\phi}$ , normalized by  $\nu_t \Omega_\odot$ , during magnetic maximum (left two panels) and minimum (right two panels).

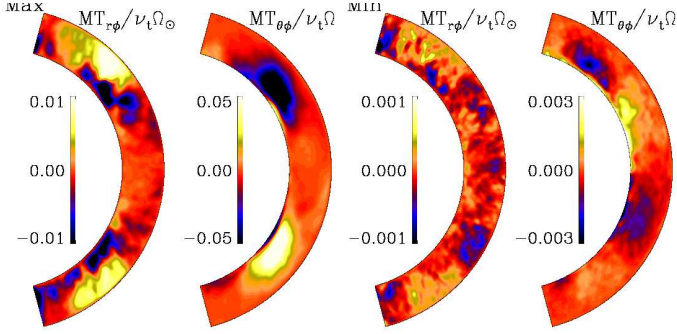


**Fig. 17.** From Run A: Components of the magnetic tension  $MT_{r\phi} = \overline{B_\phi \overline{B_r}} / \rho \mu_0$  and  $MT_{\theta\phi} = \overline{B_\phi \overline{B_\theta}} / \rho \mu_0$ , normalized by  $\nu_t \Omega_\odot$ , during magnetic maximum (left two panels) and minimum (right two panels).

minimum, which is why we show in Fig. 15 averages over all time. Another important property is that  $\Lambda_V$  is of the same order as  $\nu_t$ , which is consistent with earlier findings (Käpylä et al. 2010a). We find that for both Runs A and E,  $\Lambda_H$  is positive which is again in agreement with the analytical results. By comparing the present results with the hydrodynamic counterparts of Käpylä et al. (2014), we find that the  $\Lambda$ -effect, particularly in AS cases (Run A), is much weaker. This could be a reason of getting much suppressed differential rotation, compared to the hydrodynamic simulations, particularly in AS cases (Runs A–C); see Fig. 3. Furthermore we see a significant cycle-related variation in the  $\Lambda$ -effect. In AS cases, both  $\Lambda_V$  and  $\Lambda_H$  are much smaller during cycle maximum (see last two columns in Fig. 14). This is possibly the reason for significant temporal variations in the large-scale flow.

Finally, we compute the radial and latitudinal components of the Maxwell stress:  $M_{r\phi} = \overline{B'_r B'_\phi} / \rho \mu_0$  and  $M_{\theta\phi} = \overline{B'_\theta B'_\phi} / \rho \mu_0$ , respectively. Figure 16 shows these profiles in the meridional plane from Run A, both during magnetic maximum and minimum. Note that  $M_{r\phi}$  and  $M_{\theta\phi}$  are normalized by  $\nu_t \Omega_\odot$  using the  $\nu_t$  computed earlier. We see that both  $M_{r\phi}$  and  $M_{\theta\phi}$  are an order of magnitude smaller than  $Q_{r\phi}$  and  $Q_{\theta\phi}$  and they have the same signs as  $Q_{r\phi}$  and  $Q_{\theta\phi}$ , respectively. During magnetic maximum, both  $M_{r\phi}$  and  $M_{\theta\phi}$  (left two panels of Fig. 16) are significantly larger than during minimum (left two panels). Therefore the Maxwell stresses may be a source of the temporal variation in the differential rotation.

The Maxwell stress discussed above contributes to the redistribution of angular momentum by fluctuating (non-axisymmetric) magnetic fields. The mean axisymmetric fields also contribute to the angular momentum balance. This mean contribution is the result of correlations of the mean toroidal field with the radial and latitudinal components of the mean magnetic fields which are  $MT_{r\phi} = \overline{B_\phi \overline{B_r}} / \rho \mu_0$  and  $MT_{\theta\phi} = \overline{B_\phi \overline{B_\theta}} / \rho \mu_0$ . In Fig. 17, we show these two terms from Run A, both during magnetic maximum and minimum. We see that both are much smaller than the convective Reynolds stresses  $Q_{r\phi}$  and  $Q_{\theta\phi}$  and comparable to the fluctuating contributions  $M_{r\phi}$  and  $M_{\theta\phi}$  (Fig. 16). Importantly they have large temporal variations, becoming weaker during magnetic minimum.

## 5. Conclusion

We have revisited the recently discovered bistability of stellar differential rotation in hydrodynamic spherical convection simulations (Gastine et al. 2014; Käpylä et al. 2014). Except for the allowance of dynamo-generated magnetic fields, our models are essentially the same as those of Käpylä et al. (2014). By taking different radiative conductivities, the convective velocities and hence the rotational influence are varied in the simulations. Runs A, B, and BC ( $Co = 1.34, 1.35$ , and  $1.38$ ) produce AS differential rotation, whereas Runs C, D, and E ( $Co = 1.44, 1.67$ , and  $1.75$ ) produce SL differential rotation. When we take an AS (SL) rotation profile as initial condition and perform a set of simulations by increasing (decreasing) the radiative conductivity slowly, we find similar states of differential rotation as in simulations which were started from scratch, i.e., with an initially rigid rotation profile. Therefore the bistable states of differential rotation seem to disappear in the MHD simulations.

Besides the disappearance of the bistable differential rotation in MHD simulations, we find several other new results. (i) The abrupt transition from AS to SL rotation in hydrodynamic simulations now seems to become more gradual and this transition happens at slightly smaller values of  $Ro_c$  ( $\approx 0.66$ ) and thus smaller values of  $Co$  ( $\approx 1.4$ ). This means that the magnetic field helps to produce SL differential rotation, which is also in agreement with the recent study of Fan & Fang (2014). (ii) The polar vortices or jet-like structures that were observed in previous hydrodynamic simulations (e.g., Heimpel & Aurnou 2007; Käpylä et al. 2014) are now absent. (iii) Both differential rotation and meridional circulation are now strongly suppressed compared to the hydrodynamic values and lie within the observed range. The suppression of these large-scale flows in the magnetic runs, particularly in AS differential rotation cases, could be the consequences of a strong reduction of the  $\Lambda$  effect and the presence of the Lorentz force of the large-scale magnetic field on the flow (Malkus & Proctor 1975). (iv) The large-scale flows show significant time variation as a consequence of the magnetic cycles. All cases with AS differential rotation (Runs A–BC) show clear magnetic cycles and their large-scale flows have cycle-related variations. Run A, which is more solar-like in terms of its highest convective flux and lowest  $Co$  value, shows  $\approx 6\%$  variation in  $\Omega$  about its mean. However the variation in meridional circulation is as large as  $65\%$  and in large-scale shear the variation is about  $75\%$ . All runs which produce SL differential rotation (Runs C–E)

also show some magnetic cycles, although they are not so regular and prominent as for AS differential rotation. In these runs we also see a detectable temporal variation in the large-scale flows. For Run E, which has the smallest convective flux and SL differential rotation, the variation in  $\Omega$  is about 5%, whereas the variation in both meridional circulation and large-scale shear is about 50%.

Many authors simulate the large-scale flows in stellar convection zones using hydrodynamical models assuming that the magnetic field does not have a significant effect (Ballot et al. 2007; Gastine et al. 2013, 2014; Guerrero et al. 2013; Käpylä et al. 2014, to mention just a few). It is difficult to quantify the effects of dynamo-generated magnetic fields on flows in the Sun from simulations as all the existing models are still far from the real Sun. However, from observations (Chou & Dai 2001; Hathaway & Rightmire 2010; Antia et al. 2008) we do see significant variations in both meridional circulation and rotational shear as well as a small variation of differential rotation in the form of torsional oscillations, which are believed to be (at least partially) coming from cyclic variations of the magnetic fields. The present study now suggests that magnetic fields cannot be neglected in simulating the large-scale flows in solar convection zone.

**Acknowledgements.** We thank Jörn Warnecke for a careful reading the manuscript and suggesting corrections. BBK wishes to thank University of Helsinki, Finland for a warm hospitality there where this work was initiated. Financial support from the Academy of Finland grants No. 136189, 140970, 272786 (PJK) and 272157 to the ReSoLVE Centre of Excellence (MJM), as well as the Swedish Research Council grants 621-2011-5076 and 2012-5797, and the European Research Council under the AstroDyn Research Project 227952 are acknowledged as well as the HPC-Europa2 project, funded by the European Commission - DG Research in the Seventh Framework Programme under grant agreement No. 228398. The computations have been carried out at the National Supercomputer Centres in Linköping and Umeå and the Center for Parallel Computers at the Royal Institute of Technology in Sweden, the Nordic High Performance Computing Center in Iceland, and the supercomputers hosted by CSC – IT Center for Science in Espoo, Finland.

## References

- Antia, H. M., Basu, S., & Chitre, S. M. 2008, *ApJ*, 681, 680  
 Augustson, K., Brun, A. S., Miesch, M. S., & Toomre, J. 2013, *arXiv:1310.8417*  
 Ballot, J., Brun, A. S., & Turck-Chièze, S. 2007, *ApJ*, 669, 1190  
 Brandenburg, A., Chan, K. L., Nordlund, Å., & Stein, R. F. 2005, *AN*, 326, 681  
 Brandenburg, A., Moss, D., & Tuominen, I. 1992, *A&A*, 265, 328  
 Brandenburg, A., Saar, S. H., & Turpin, C. R. 1998, *ApJ*, 498, L51  
 Brown, B. P., Browning, M. K., Brun, A. S., Miesch, M. S., & Toomre, J. 2010, *ApJ*, 711, 424  
 Brown, T. M., Christensen-Dalsgaard, J., Dziembowski, W. A., et al. 1989, *ApJ*, 343, 526  
 Brun, A. S., Miesch, M. S., & Toomre, J. 2004, *ApJ*, 614, 1073  
 Brun, A. S. & Palacios, A. 2009, *ApJ*, 702, 1078  
 Chan, K. L. 2010, in *IAU Symposium*, Vol. 264, IAU Symposium, ed. A. G. Kosovichev, A. H. Andrei, & J.-P. Rozelot, 219–221  
 Chou, D.-Y. & Dai, D.-C. 2001, *ApJ*, 559, L175  
 Choudhuri, A. R., Schüssler, M., & Dikpati, M. 1995, *A&A*, 303, L29  
 Cole, E., Käpylä, P. J., Mantere, M. J., & Brandenburg, A. 2014, *ApJL*, 780, L22  
 Dikpati, M. & Charbonneau, P. 1999, *ApJ*, 518, 508  
 Fan, Y. & Fang, F. 2014, *ApJ*, 789, 35  
 Gastine, T., Wicht, J., & Aurnou, J. M. 2013, *Icarus*, 225, 156  
 Gastine, T., Yadav, R. K., Morin, J., Reiners, A., & Wicht, J. 2014, *MNRAS*, 438, L76  
 Ghizaru, M., Charbonneau, P., & Smolarkiewicz, P. K. 2010, *ApJ*, 715, L133  
 Gilman, P. A. 1977, *Geophys. Astrophys. Fluid Dynam.*, 8, 93  
 Gilman, P. A. 1983, *ApJS*, 53, 243  
 Guerrero, G., Smolarkiewicz, P. K., Kosovichev, A. G., & Mansour, N. N. 2013, *ApJ*, 779, 176  
 Hathaway, D. H. & Rightmire, L. 2010, *Science*, 327, 1350  
 Hazra, G., Karak, B. B., & Choudhuri, A. R. 2014, *ApJ*, 782, 93  
 Heimpel, M. & Aurnou, J. 2007, *Icarus*, 187, 540  
 Hotta, H. & Yokoyama, T. 2011, *ApJ*, 740, 12  
 Käpylä, P. J. & Brandenburg, A. 2008, *A&A*, 488, 9  
 Käpylä, P. J., Brandenburg, A., Korpi, M. J., Snellman, J. E., & Narayan, R. 2010a, *ApJ*, 719, 67  
 Käpylä, P. J., Korpi, M. J., Brandenburg, A., Mitra, D., & Tavakol, R. 2010b, *Astron. Nachr.*, 331, 73  
 Käpylä, P. J., Korpi, M. J., & Tuominen, I. 2004, *A&A*, 422, 793  
 Käpylä, P. J., Korpi, M. J., & Tuominen, I. 2006, *Astron. Nachr.*, 327, 884  
 Käpylä, P. J., Mantere, M. J., & Brandenburg, A. 2011a, *Astron. Nachr.*, 332, 883  
 Käpylä, P. J., Mantere, M. J., & Brandenburg, A. 2012, *ApJ*, 755, L22  
 Käpylä, P. J., Mantere, M. J., & Brandenburg, A. 2014, *A&A*, in press, *arXiv:1401.2981*  
 Käpylä, P. J., Mantere, M. J., Cole, E., Warnecke, J., & Brandenburg, A. 2013, *ApJ*, 778, 41  
 Käpylä, P. J., Mantere, M. J., Guerrero, G., Brandenburg, A., & Chatterjee, P. 2011b, *A&A*, 531, A162  
 Karak, B. B. 2010, *ApJ*, 724, 1021  
 Karak, B. B. & Choudhuri, A. R. 2011, *MNRAS*, 410, 1503  
 Karak, B. B. & Choudhuri, A. R. 2012, *Sol. Phys.*, 278, 137  
 Karak, B. B. & Choudhuri, A. R. 2013, *Research in Astronomy and Astrophysics*, 13, 1339  
 Karak, B. B., Kitchatinov, L. L., & Choudhuri, A. R. 2014, *ArXiv e-prints*  
 Kitchatinov, L. L. & Oleskoy, S. V. 2011, *MNRAS*, 411, 1059  
 Kitchatinov, L. L., Pipin, V. V., Makarov, V. I., & Tlatov, A. G. 1999, *Sol. Phys.*, 189, 227  
 Kitchatinov, L. L. & Rüdiger, G. 1995, *A&A*, 299, 446  
 Kitchatinov, L. L. & Rüdiger, G. 2004, *Astron. Nachr.*, 325, 496  
 Kitchatinov, L. L. & Rüdiger, G. 2005, *Astron. Nachr.*, 326, 379  
 Kitchatinov, L. L., Rüdiger, G., & Küker, M. 1994, *A&A*, 292, 125  
 Küker, M., Arlt, R., & Rüdiger, G. 1999, *A&A*, 343, 977  
 Küker, M. & Rüdiger, G. 2011, *Astron. Nachr.*, 332, 933  
 Malkus, W. V. R. & Proctor, M. R. E. 1975, *J. Fluid Mech.*, 67, 417  
 Matt, S. P., Do Cao, O., Brown, B. P., & Brun, A. S. 2011, *Astron. Nachr.*, 332, 897  
 Miesch, M. S., Brun, A. S., & Toomre, J. 2006, *ApJ*, 641, 618  
 Nelson, N. J., Brown, B. P., Brun, A. S., Miesch, M. S., & Toomre, J. 2013, *ApJ*, 762, 73  
 Pipin, V. V. & Kosovichev, A. G. 2011, *ApJ*, 727, L45  
 Pulkkinen, P., Tuominen, I., Brandenburg, A., Nordlund, A., & Stein, R. F. 1993, *A&A*, 267, 265  
 Racine, É., Charbonneau, P., Ghizaru, M., Bouchat, A., & Smolarkiewicz, P. K. 2011, *ApJ*, 735, 46  
 Rempel, M. 2005, *ApJ*, 622, 1320  
 Rempel, M. 2006, *ApJ*, 647, 662  
 Rieutord, M., Brandenburg, A., Mangeney, A., & Drossart, P. 1994, *A&A*, 286, 471  
 Rüdiger, G. 1980, *Geophys. Astrophys. Fluid Dynam.*, 16, 239  
 Rüdiger, G. 1989, *Differential Rotation and Stellar Convection. Sun and Solar-type Stars* (Berlin: Akademie Verlag)  
 Rüdiger, G., Egorov, P., & Ziegler, U. 2005, *Astron. Nachr.*, 326, 315  
 Saar, S. H. & Brandenburg, A. 1999, *ApJ*, 524, 295  
 Schad, A., Timmer, J., & Roth, M. 2013, *ApJ*, 778, L38  
 Schou, J., Antia, H. M., Basu, S., et al. 1998, *ApJ*, 505, 390  
 Schrunner, M., Rädler, K.-H., Schmitt, D., Rheinhardt, M., & Christensen, U. 2005, *Astron. Nachr.*, 326, 245  
 Schrunner, M., Rädler, K.-H., Schmitt, D., Rheinhardt, M., & Christensen, U. R. 2007, *Geophys. Astrophys. Fluid Dynam.*, 101, 81  
 Schüssler, M. 1979, *A&A*, 72, 348  
 Strassmeier, K. G., Kratzwald, L., & Weber, M. 2003, *A&A*, 408, 1103  
 Thompson, M. J., Christensen-Dalsgaard, J., Miesch, M. S., & Toomre, J. 2003, *ARA&A*, 41, 599  
 Warnecke, J., Käpylä, P. J., Mantere, M. J., & Brandenburg, A. 2013, *ApJ*, 778, 141  
 Weber, M., Strassmeier, K. G., & Washuettl, A. 2005, *Astron. Nachr.*, 326, 287  
 Zhao, J., Bogart, R. S., Kosovichev, A. G., Duvall, Jr., T. L., & Hartlep, T. 2013, *ApJ*, 774, L29